OPEN ACCESS

ARTICLE

Innovative biogas reforming in catalytic membrane reactor for CO-free green hydrogen production with carbon capture

Mengke Liu,[1,2,3] Tianmiao Hu,[1,2] Yan Zhang,[1,2,*] Zhengwen Cao,[1,2] Lujian Jia,[1,2] Wenyuan Liang,[1,2] Alexander Nemudry,[4] and Heqing Jiang[1,2,*]

*Correspondence: E-mail: zhangyan@qibebt.ac.cn (Y. Z.); jianghq@qibebt.ac.cn (H. J.)

Received: June 24, 2025; Accepted: September 19, 2025; https://doi.org/10.59717/j.xinn-energy.2025.100119

GRAPHICAL ABSTRACT

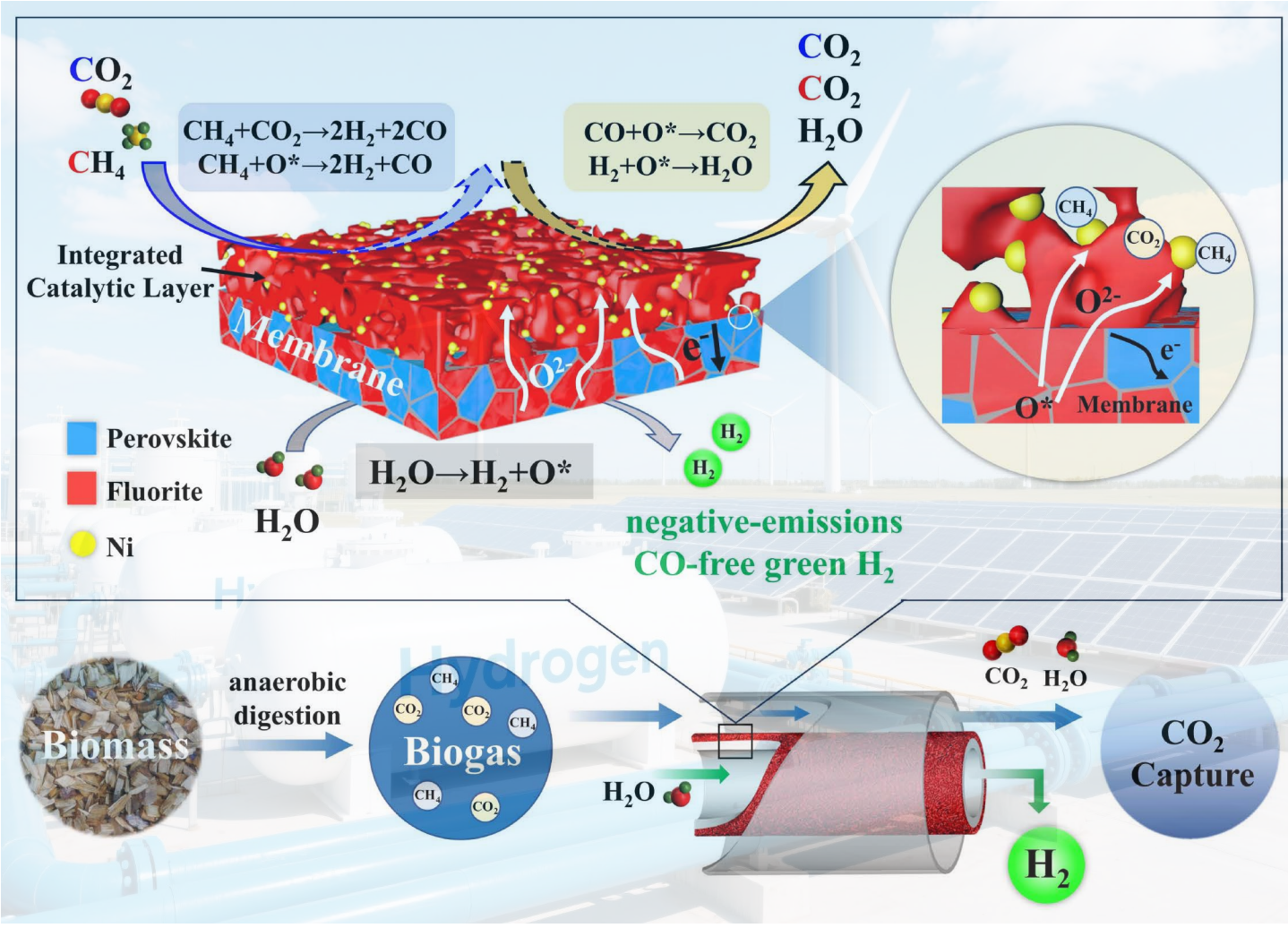

PUBLIC SUMMARY

- An innovative strategy for one-step CO-free H_2 production from biogas was proposed.
- The $Ce_{0.8}Sm_{0.15}Ni_{0.05}O_{2-\delta}$ catalytic layer was compatible with the ceramic membrane.
- An accumulative production rate of 10.35 mL min^{-1} cm^{-2} of CO-free H_2 was achieved.
- A remarkably high hydrogen yield of 94.5% was achieved.

ARTICLE

OPEN ACCESS

Innovative biogas reforming in catalytic membrane reactor for CO-free green hydrogen production with carbon capture

Mengke Liu,[1,2,3] Tianmiao Hu,[1,2] Yan Zhang,[1,2,*] Zhengwen Cao,[1,2] Lujian Jia,[1,2] Wenyuan Liang,[1,2] Alexander Nemudry,[4] and Heqing Jiang[1,2,*]

[1]Key Laboratory of Photoelectric Conversion and Utilization of Solar Energy, Qingdao New Energy Shandong Laboratory, Qingdao Institute of Bioenergy and Bioprocess Technology, Chinese Academy of Sciences, Qingdao 266101, China

[2]Shandong Energy Institute, Qingdao 266101, China

[3]University of Chinese Academy of Sciences, Beijing 100049, China

[4]Institute of Solid State Chemistry and Mechanochemistry of the Siberian Branch of the Russian Academy of Sciences, Novosibirsk 630090, Russia

*Correspondence: E-mail: zhangyan@qibebt.ac.cn (Y. Z.); jianghq@qibebt.ac.cn (H. J.)

Received: June 24, 2025; Accepted: September 19, 2025; https://doi.org/10.59717/j.xinn-energy.2025.100119

Citation: Liu M., Hu T., Zhang Y., et al. (2025). Innovative biogas reforming in catalytic membrane reactor for CO-free green hydrogen production with carbon capture. *The Innovation Energy* **2**:100119.

Biogas reforming is an attractive process for green hydrogen production; however, CO residual in the obtained hydrogen is usually eliminated by multiple post-treatment units. Herein, we report an innovative route by coupling water splitting with biogas reforming in a catalytic membrane reactor to directly produce CO-free H_2 and capture CO_2 on opposite sides of the membrane. Notably, a hollow fiber composite membrane consisting of doped ceria and perovskite is employed, integrated with porous catalytic layer $Ce_{0.8}Sm_{0.15}Ni_{0.05}O_{2-\delta}$ over which Ni nanoparticles can be *in-situ* exsolved. The catalytic layer's compatibility with the ceramic membrane ensures low ionic resistance and effective reaction-diffusion synergy. An accumulative production rate of 10.35 mL min^{-1} cm^{-2} of CO-free H_2 was achieved from water splitting on the core side, while biogas reforming produced CO_2 on the opposite side which was ready for capture. This work provides an alternative option for utilizing sustainable bioenergy to produce negative-emissions green hydrogen.

INTRODUCTION

Green hydrogen with negative CO_2 emissions generated from sustainable bioenergy sources, such as biomass, bioethanol, and biogas, has garnered significant interest, given by the depletion of fossil fuels and the pressing imperative to combat global climate change.[1-6] However, the production of environmentally friendly hydrogen with negative CO_2 emissions for subsequent applications, such as fuel cells, involves a three-step process: i) utilizing thermochemical processes (e.g., dry reforming of methane (DRM): $CH_4(g)+CO_2(g)\rightarrow 2CO(g)+2H_2(g)$) to produce hydrogen; ii) ensuring complete elimination of even minute traces of CO, as their presence (≥10 ppm) can significantly impair the Pt electrocatalyst in proton exchange membrane fuel cells;[1,7-9] iii) employing post-treatment units to separate hydrogen and CO_2.[10-15] Although the concept of generating CO-free green hydrogen with carbon capture directly from renewable bioenergy in a single step, rather than three steps, is attractive, it presents significant challenges.[4,16]

Several methods have been suggested for converting methane into different resources in membrane reactors. While a palladium-based hydrogen-permeable membrane enables the direct extraction of pure hydrogen from methane through DRM,[17-19] it comes with high costs attributed to the precious metal Pd. Oxygen-permeable membranes provide the opportunity to simultaneously produce syngas from methane and CO-free hydrogen from water.[20-25] When both sides of the catalytic membrane are exposed to water and methane respectively, the H_2O undergoes a splitting process into H_2 and O_2. The oxygen species then diffuse as O^{2-} and are consumed by the methane over the catalytic layer on the opposite side of the membrane, resulting in syngas through partial oxidation of methane (POM, $CH_4+1/2O_2\rightarrow CO+2H_2$).[26] Once the O_2 is transferred to the other side and utilized to convert methane to syngas, the H_2 is obtained on the water-splitting side. The productivity of hydrogen of such reactors is typically constrained by poor stability resulting from the incompatibility between catalysts and membranes. This includes: i) The failure of membrane materials due to reactions between the packed heterogeneous catalytic layers,[27-32] such as Ni/Al_2O_3,[28] Pt/SiO_2,[3] Ni/ZrO_2,[30] and Co- or Fe-based perovskite-containing oxygen-permeable membrane materials. ii) The formation of non-conductive phases, such as insulating barium-silicon oxide layers, which hinder the surface reactive sites and disrupt the transport of electrons and oxygen ions, thereby reducing the oxygen permeation flux and limit hydrogen productivity.[33] More critically, when processing real biogas (CH_4/CO_2 mixtures), conventional oxygen-transporting membranes face two fundamental limitations, including the CO_2-induced membrane degradation through carbonate formation, and unutilized CO_2 acting as inert diluent that suppresses methane conversion efficiency. Therefore, it is highly imperative to elaborate catalytic layers and develop chemically stable (towards both CO_2 and reducing agents) catalytic membrane reactors for the production of CO-free green hydrogen from renewable bioenergy.

In this work, we redefine the role of CO_2 in membrane reactors by transforming it from a stability-threatening impurity to an active reforming agent. In stark contrast to previous methane/water systems, an innovative biogas reforming strategy for highly efficient CO-free green hydrogen production with carbon capture is showcased through a specially designed membrane reactor (Figure 1). On the biogas side, dry reforming alongside POM occurs, creating self-regulating oxygen potential that suppresses carbon deposition. On the other side, permeated oxygen ions (O^{2-}) drive water splitting to pure H_2. This paradigm shift demands materials innovation to address inherent stability challenges. In this regard, we engineer a hollow fiber catalytic membrane reactor (CSO-Ni@CSO-SSTF) comprising a CO_2-tolerant dual-phase membrane ($Ce_{0.8}Sm_{0.2}O_{2-\delta}$-$Sm_{0.2}Sr_{0.8}Ti_{0.4}Fe_{0.6}O_{3-\delta}$ (CSO-SSTF)) and a self-regenerative $Ce_{0.8}Sm_{0.15}Ni_{0.05}O_{2-\delta}$ (CSO-Ni) porous catalytic layer, where *in-situ* exsolved Ni nanoparticles dynamically suppress coking. The excellent compatibility and stability of CSO-Ni and CSO-SSTF effectively prevents material failure and facilitates the efficient transfer of oxygen ions, enhancing hydrogen productivity. Consequently, an accumulated production rate of 10.35 mL min^{-1} cm^{-2} of CO-free H_2 was achieved from water splitting, representing up to 94.5% of the theoretical overall hydrogen yield ($CH_4 + 2H_2O = 4H_2 + CO_2$). By integrating biogas reforming, water splitting, and carbon capture into a single reactor, this work establishes a scalable pathway for renewable hydrogen production aligned with net-negative emissions targets.

MATERIALS AND METHODS

Preparation of catalysts and hollow fiber oxygen-permeable composite membranes

$Ce_{0.8}Sm_{0.15}Ni_{0.05}O_{2-\delta}$ (CSO-Ni) catalyst was prepared based on the combined citric acid and ethylenediaminetetraacetic acid (EDTA) method. Specifically, stoichiometric amounts of $Ni(NO_3)_2{\cdot}6H_2O$, $Sm(NO_3)_3{\cdot}6H_2O$ and $Ce(NO_3)_3{\cdot}6H_2O$ were dissolved in de-ionized water, followed by the addition of EDTA and citric acid according to the molar ratio of EDTA: citric acid: total of metal cations of 1:1.5:1. Then, the pH value of the solution was adjusted to about 9 using ammonia solution. The mixed solution was stirred overnight and then heated at 120-150 °C for 3 hours to obtain a gel, which was calcined at 800 °C for 5 h to prepare CSO-Ni catalyst.

The Ni/Al_2O_3 catalyst was prepared via a wetness impregnation method. A commercial γ-Al_2O_3 support (9.83 g) was impregnated with 10 mL of a 0.289 mol/L aqueous $Ni(NO_3)_2$ solution. After drying overnight at 110 °C, the material was calcined in air at 650 °C for 4 hours, yielding a catalyst with a nickel loading of 1.7 wt%.

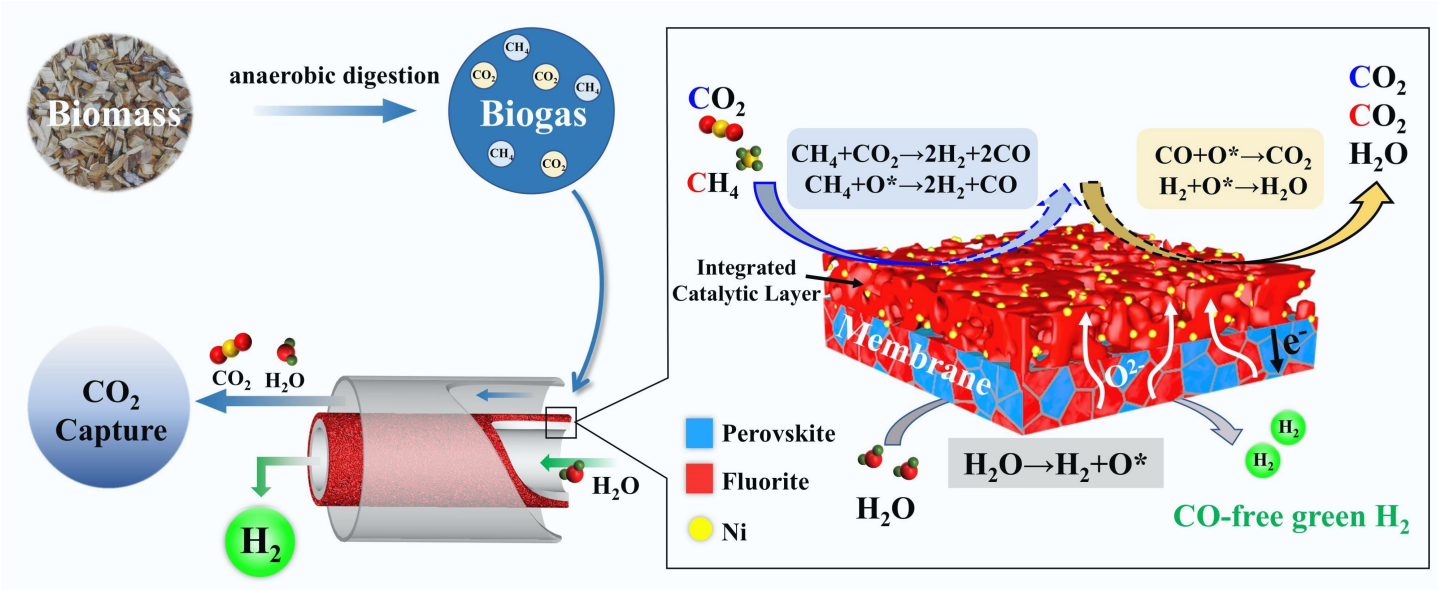

Figure 1. Schematic diagram of CO-free green hydrogen production with carbon capture in a membrane reactor by coupling water splitting with biogas reforming.

The 60 mol% $Ce_{0.8}Sm_{0.2}O_{2-\delta}$-40 mol% $Sm_{0.2}Sr_{0.8}Ti_{0.4}Fe_{0.6}O_{3-\delta}$ (CSO-SSTF) hollow fiber membrane was prepared following the phase conversion and sintering method. To produce the hollow fiber membrane slurry, CeO_2, Sm_2O_3, $SrCO_3$, Fe_2O_3, and TiO_2 were precisely weighed according to their stoichiometric ratios and introduced into a zirconia ball-milling jar. Deionized water functioned as the wet-grinding medium, with zirconia balls utilized for grinding. The mixture underwent milling at 500 rpm for 24 h. Subsequently, the slurry was dried in an oven for 12 h to yield the CSO-SSTF precursor powder. After that, a casting solution was prepared by ball-milling a mixture of 6 wt% polyethersulfone (PESF, A-300, BASF), 30 wt% N-methylpyrrolidone (NMP, AR grade, purity >99.8%), and 65 wt% fine powders in a zirconia ball mill jar at 500 rpm for 3 h, ensuring uniform dispersion of the polymer and powder components. Subsequently, the casting solution was transferred into the feed tank of a lab-fabricated hollow fiber membrane production system, and the slurry inside the tank was pressurized to 0.4 bar using an air cylinder. The hollow fiber precursor was prepared using a spinneret with an outer diameter of 1.5 mm and an inner diameter of 1.0 mm. Deionized water and tap water were used as the internal and external coagulants, respectively. The resultant hollow fiber precursors were immersed in a deionized water bath at room temperature for further solidification. The solidified hollow fiber precursors were cut into 0.5 m pieces and sintered at 1500 °C for 10 h in air to obtain gas-tight membrane. Eventually, the CSO-Ni or Ni/Al_2O_3 catalyst powders were blended with water to create a viscous slurry. This slurry was subsequently applied onto the gas-tight membrane surface via brushing. The coated catalyst layer was then sintered at 1100 °C for 1 hour to enhance the interfacial adhesion between the catalyst and the membrane surface. Consequently, the CSO-SSTF hollow fiber composite membrane integrated with CSO-Ni (namely CSO-Ni@CSO-SSTF) or packed with Ni/Al_2O_3 catalyst (namely Ni/Al_2O_3@CSO-SSTF) could be obtained. The preparation method for the 60 mol% $Ce_{0.85}Sm_{0.15}O_{2-\delta}$-40 mol% $Sm_{0.6}Sr_{0.4}Al_{0.3}Fe_{0.7}O_{3-\delta}$ (CSO-SSAF) hollow fiber membrane mirrors the core steps used for the CSO-SSTF hollow fiber membrane described earlier. The difference lies in the precursor material composition and sintering parameters. This method employs CeO_2, Sm_2O_3, $SrCO_3$, Fe_2O_3, and Al_2O_3 oxide powders as raw materials, with the solidified hollow fiber precursors being sintered at 1450 °C for 10 hours to produce the CSO-SSAF membrane.

Characterization

The X-ray diffraction (XRD) pattern was recorded on Bruker D8 ADVANCE diffractometer. The microscopic morphology and energy-dispersive X-ray spectroscopy (EDXs) analyses were conducted using Thermo Scientific Prisma E and ZEISS Sigma 500 scanning electron microscopes (SEM). A high resolution-transmission electron microscope (HR-TEM, FEI Tecnai G2 F30) was employed to investigate the microstructures. High-angle annular dark-field scanning transmission electron microscopy (HAADF-STEM) was performed on Talos F200X with Super-X EDS. X-ray photoelectron spectroscopy (XPS) was conducted on a Thermo ESCALAB 250Xi model X-ray photoelectron spectrometer instrument (Al Ka radiation, hv = 1486.6 eV, 150W) to analyze the surface of the CSO-SSTF materials and CSO-Ni catalyst.

H_2 temperature programmed reduction (H_2-TPR) and O_2 temperature programmed oxidization (O_2-TPO) were performed on a Micromeritics AutoChem II 2920 instrument. For H_2-TPR, after a standard cleaning pretreatment, 100 mg of catalyst in a U tube reactor was heated from room temperature to 950 °C with a heating rate of 10 °C·min^{-1} in a flow of 10% H_2/Ar (50 mL min^{-1}). For the spent catalyst, O_2-TPO was investigated and the processes were similar with H_2-TPR except for the replacement of 10 vol % H_2/Ar with 5 vol % O_2/Ar.

CH_4 temperature programmed surface reaction (CH_4-TPSR) was carried out using a Micromeritics AutoChem II 2920 instrument connected with online mass spectrum (MS, ThermoStar GSD 301 T2). The catalyst was reduced in a quartz reactor at 800 °C for 2 h using 10% H_2/Ar with 30 mL min^{-1}. The quartz reactor was cooled down to the room temperature in He with 30 mL min^{-1}. After the sample was cooled to 50 °C, the sample was heated from 50 to 950 °C at 10 °C min^{-1} in flowing 50% CH_4/Ar. The effluent of H_2, CH_4, CO_2, and CO with the signals of m/e = 2, 15, 44 and 28 were detected by MS. CO_2 temperature programmed surface reaction (CO_2-TPSR) experiment was similar with CH_4-TPSR except for the replacement of 50% CH_4/Ar with 10 vol % CO_2/He. The effluent of O_2, CO_2 and CO with the signals of m/e = 32, 44 and 28 were detected by MS.

Water splitting and biogas reforming in the membrane reactor

CO-free green hydrogen production by combining water splitting with biogas reforming was realized in a self-made hollow fiber membrane reactor. The hollow fiber oxygen-permeable membrane integrated with CSO-Ni or packed with Ni/Al_2O_3 catalyst was housed in an alumina tube (6 mm diameter and 250 mm length) with a fluorine rubber seal ring. The membrane reactor was positioned in a tubular furnace with a diameter of 20 mm and a total length of 200 mm. The effective heating zone of the furnace was 5 cm, within which the hollow fiber membrane was placed. The membrane had its ends sealed with silver paste, leaving an effective length of 3 cm exposed within the heating zone, ensuring a uniform temperature profile across this exposed membrane section. 10% H_2/He with 20 mL min^{-1} was fed in the shell side at 800 °C for 2 h to drive the exsolution of Ni. Then, the CH_4, CO_2 and N_2, as the sweep gas, were introduced in the shell side, while the water and He were flowed into the core side. The helium and CO_2 flow rates could be effectively

controlled by the gas mass flow controllers (Bronkhorst, Germany). The methane and nitrogen flow rates could be adjusted by the mass flow controllers (Seven Star, China). Before use, all gas mass flow controllers required to be calibrated using a soap bubble flow meter. The compositions of the effluent gases were detected online using Agilent 7890 gas chromatograph fitted with a TCD detector. Specifically, the core-side effluent was analyzed for hydrogen (H_2) production and potential shell-side-permeated nitrogen (N_2), while the shell-side effluent was analyzed for reaction products including methane (CH_4), carbon dioxide (CO_2), carbon monoxide (CO), hydrogen (H_2), and nitrogen (N_2). Water was removed via a condenser prior to analysis and was not quantified in the chromatographic measurements. In addition, the trace CO concentration on the water-splitting side was determined using a gas chromatograph equipped with a flame ionization detector (GC-FID).

The CH_4 conversion (X_{CH4}), CO_2 conversion (X_{CO2}), CO selectivity (S_{CO}), CO_2 selectivity (S_{CO2}) and hydrogen production rate J_{H2} were calculated using the following equations:

$$X_{CH_4}=\frac{F^{in}_{CH_4}-F^{out}_{CH_4}}{F^{in}_{CH_4}}\times 100\%$$

$$X_{CO_2}=\frac{F^{in}_{CO_2}-F^{out}_{CO_2}}{F^{in}_{CO_2}}\times 100\%$$

$$S_{CO}=\frac{F^{out}_{CO}}{F^{in}_{CH_4}+F^{in}_{CO_2}-F^{out}_{CH_4}-F^{out}_{CO_2}}\times 100\%$$

$$S_{CO_2}=\frac{F^{out}_{CO_2}}{F^{in}_{CH_4}+F^{in}_{CO_2}}\times 100\%$$

$$J_{H_2}=\frac{F^{out}_{H_2}-F^{out}_{H_2,leak}}{A}$$

$$F^{out}_{H_2,leak}=\frac{C_{H_2,Shell\ side}}{C_{N_2,Shell\ side}}\times\sqrt{\frac{M_{N_2}}{M_{H_2}}}\times C_{N_2,\ core\ side}\times F$$

$$X_{CH_4}(\text{contribution of DRM})=\frac{F^{in}_{CO_2}-F^{out}_{CO_2}}{F^{in}_{CH_4}}\times 100\%$$

$$X_{CH_4}(\text{contribution of POM})=\frac{F^{in}_{CH_4}-F^{out}_{CH_4}}{F^{in}_{CH_4}}\times 100\%-X_{CH_4}(\text{contribution of DRM})$$

where F_i is the flow rate of species i, C_i is the concentration of species i and A is the effective area (1.1 cm^2) of the membrane.

RESULTS AND DISCUSSION

Structural analysis. A CSO-SSTF dual-phase hollow fiber membrane, characterized by its typical finger-like structure, was meticulously prepared to facilitate selective oxygen permeation (Figures S1-S3). This membrane serves as the foundation of the CSO-Ni@CSO-SSTF catalytic membrane reactor, fabricated by integrating a porous CSO-Ni catalytic layer over the surface of the CSO-SSTF oxygen-permeable membrane. As illustrated in Figures 2A & B, the CSO-Ni catalytic layer, with a thickness of approximately 20 μm, is closely adhered to the dense membrane, exhibiting no signs of corrosion or impurities at the interface (Figure S2). This seamless integration highlights excellent chemical compatibility between the catalytic layer and the membrane, which is crucial for maintaining long-term stability and performance. In contrast to traditional Ni-supported catalysts, where Ni nanoparticles often suffer from agglomeration due to weak metal-oxide interactions, leading to coke deposition and degradation of catalytic performance, this study employs an *in-situ* exsolution strategy to produce Ni nanoparticles. This approach effectively overcomes the durability issues associated with conventional catalysts. The crystalline structures of both the prepared and reduced CSO-Ni catalyst were thoroughly characterized using X-ray diffraction (XRD), with the results presented in Figure 2C. A new peak corresponding to metallic Ni emerged at 2θ=44.6° in the reduced CSO-Ni sample, while no peaks for NiO were detected in the fresh CSO-Ni sample. This indicates that the Ni nanoparticles were successfully formed in a reductive H_2 atmosphere.[34] The catalytically active Ni was initially incorporated into the lattice of the fluorite host during the crystallization process and subsequently exsolved from the lattice upon 20% H_2 treatment, resulting in the formation of evenly distributed Ni nanoparticles on the CSO support.[35,36] Figure 2D presents the HAADF-STEM image and corresponding elemental mappings (Ni, Ce, and O) of the reduced CSO-Ni catalyst, revealing the presence of Ni nanoparticles with a size of approximately 30 nm, which were *in-situ* generated from the CSO-Ni material. The HR-TEM image (Figure 2E) further confirms the interplanar spacing of CSO (111) and Ni (111). The exsolved Ni nanoparticles are embedded on the surface of the parent doped ceria, forming robust metal-oxide interfaces. These strong interfaces not only enhance the dispersion and stability of the Ni nanoparticles but also facilitate efficient electron transfer and oxygen ion diffusion, which are critical for the overall catalytic performance.

Surface oxidation states. The surface oxidation states of Ni in both the as-prepared and reduced samples were meticulously analyzed using X-ray photoelectron spectroscopy (XPS). Figure 2F presents the Ni 2p3/2 spectra for the fresh and reduced CSO-Ni catalysts. In the as-prepared CSO-Ni catalyst, the peak at approximately 855.8 eV is attributed to Ni^{2+}, while the peak centered at around 860.8 eV corresponds to the Ni 2p3/2 shake-up satellite.[37] Following H_2 reduction, a new characteristic peak at 852.2 eV emerges, which is attributed to metallic Ni^0. This observation confirms the successful exsolution of Ni nanoparticles in the reduced CSO-Ni catalyst, aligning with the XRD and STEM results depicted in Figures 2C & D.[38] Notably, the presence of Ni^{2+} species in the reduced sample suggests partial re-oxidation of Ni nanoparticles upon exposure to atmospheric oxygen, likely due to the strong interactions between Ni and the doped ceria support. Figure 2G illustrates the Ce 3d spectra for both the fresh and reduced CSO-Ni catalysts. The peaks labeled V and U correspond to Ce 3d5/2 and Ce 3d3/2, respectively.[38,39] The peaks labeled V_0 and V' are attributed to Ce^{3+}, while the peaks labeled V_1, V_2 and V'' are related to Ce^{4+}. Upon reduction, the concentration of Ce^{3+} in the CSO-Ni catalyst increases from 19.6% to 33.4%, indicating a significant rise in the number of oxygen vacancies.[3] This increase in oxygen vacancies not only enhances the mobility of oxygen species but also significantly improves the catalytic performance for CO_2 adsorption and activation. To further elucidate the behavior of the CSO-Ni catalyst under reducing conditions, H_2-temperature-programmed reduction (H_2-TPR) experiments were conducted, with the results presented in Figure 2H. For the CSO support, the low-temperature peak at around 512 °C is attributed to H_2 consumption by surface-capping oxygen (Ce^{4+} to Ce^{3+}), while the high-temperature peak at around 710 °C corresponds to H_2 consumption by lattice oxygen (Ce^{4+} to Ce^{3+}), leading to the formation of oxygen vacancies that serve as active sites for CO_2 adsorption and activation.[22,40] The CSO-Ni catalyst exhibits strong reduction features at 335°C, primarily due to the exsolution of nickel from the lattice.[41] The peak at 275°C is attributed to the reduction of surface oxygen related to the substitution of Ce^{4+} by Ni^{2+} in the CeO_2 lattice.[3] Approximately 57.9 % of the initial Ni^{2+} species were reduced during the H_2-TPR process, highlighting the robust interaction between Ni and the support. The H-spillover effect over the CSO-Ni interfaces significantly enhances the hydrogen consumption, increasing from 0.21 mmol g_{cat}^{-1} for the CSO support to 0.31 mmol g_{cat}^{-1} for the CSO-Ni catalyst. Additionally, the high-temperature reduction peaks associated with cerium reduction shift to lower temperatures, indicating improved lattice oxygen mobility.[42,43] This enhanced mobility of lattice oxygen is crucial for improving the catalytic activity of the CSO-Ni catalyst, facilitating more efficient CO_2 activation and overall reaction kinetics.

Catalytic activity. The performance of the catalytic membrane reactor in producing CO-free hydrogen through the coupling of water splitting and biogas reforming was evaluated using a self-made membrane reactor integrated with the CSO-Ni catalyst (Figure 3 and Figure S4). Water and simulated biogas (CH_4 and CO_2) were introduced into the core side and shell side of the membrane, respectively. On the core side, H_2O combines with e^- and undergoes a splitting process, resulting in the formation of hydrogen and oxygen ions ($H_2O + 2e^- \rightarrow H_2 + O^{2-}$), and subsequently the generated oxygen

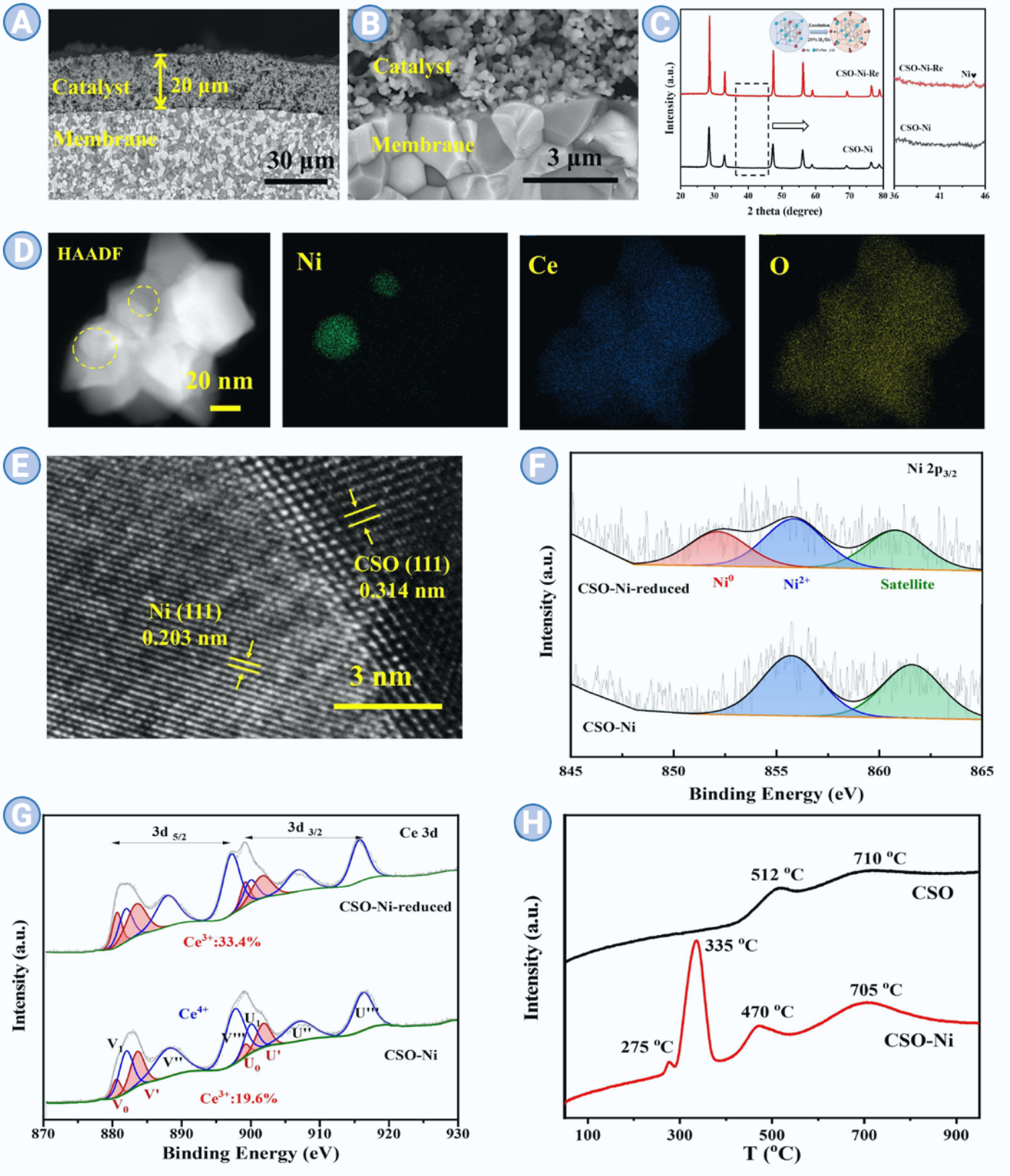

Figure 2. (A&B) The cross section SEM images of the CSO-Ni@CSO-SSTF catalytic membrane. (C) XRD patterns of the CSO-Ni catalyst before and after reduction pretreatment. (D) HAADF-STEM image and corresponding elemental mappings and (E) HR-TEM image of CSO-Ni after 20% H_2 reduction at 800 °C for 2h. XPS spectra of the fresh and the reduced CSO-Ni catalyst. (F) Ni 2p3/2, (G) Ce 3d. (H) H_2-TPR profiles of CSO-Ni catalyst and CSO support.

ions diffuse to the shell side driven by the oxygen chemical potential gradient.[26] Meanwhile, on the shell side, the dry reforming of methane (DRM, $CH_4+CO_2 \rightarrow 2CO+2H_2$) takes place over CSO-Ni catalyst to form syngas (H_2 and CO). Simultaneously, any unconverted methane reacts with the penetrated oxygen to produce additional CO, H_2 and electrons according to partial oxidation of methane (POM, $CH_4+O^{2-} \rightarrow CO+2H_2+2e^-$).[28] The electrons gener-

ated in this process migrate back to the core side to maintain local charge neutrality, ensuring the overall electrochemical balance of the system. The selective permeation of oxygen ions through the CSO-SSTF membrane ensures that the oxygen generated from water splitting is effectively utilized in the reforming process, thereby maximizing hydrogen production and guaranteeing the production of CO-free hydrogen on the water-splitting side. Figure 3A evaluates the effect of the CH_4 concentration in simulated biogas on CO-free green H_2 production. 0.5 mL min^{-1} CO_2 and 19.5 mL min^{-1} (CH_4 + N_2) were introduced into the shell side; 20 mL min^{-1} H_2O and 10 mL min^{-1} He were introduced into the core side. As the methane concentration increases from 5% to 12.5%, the CO-free green hydrogen production rate gradually increases from 0.54 mL min^{-1} cm^{-2} to 0.82 mL min^{-1} cm^{-2}. This trend indicates that higher methane concentrations enhance the contribution of POM to methane conversion, as shown in Figure 3B. The increased POM activity not only improves the overall hydrogen yield but also ensures more efficient utilization of methane, thereby enhancing the overall efficiency of the process.

To further elucidate the catalytic mechanism of our catalytic membrane, temperature programmed surface reaction (TPSR) was employed to examine the surface reaction between CH_4 and the CSO-Ni catalyst, as depicted in Figure 3C. In this experiment, the catalyst was exposed to a flow of 50% CH_4 in a helium atmosphere following *in-situ* reduction. As the temperature increases from 600 °C to 900 °C, significant CH_4 consumption and H_2 production were observed, which can be attributed to the dissociation of CH_4 on the active Ni sites ($CH_{4,(g)}+Ni^*_{(s)}$ $2H_{2,(g)}+C\times Ni^*_{(ads)}$). Simultaneously, the formation of CO occurs as a result of the carbon being oxidized by lattice oxygen species on the CSO support, following the Langmuir-Hinshelwood surface reaction mechanism ($C\times Ni^*_{(ads)}+O^*$ $CO_{(g)}+Ni^*_{(s)}+V_O$).[44,45] This process leads to the formation of oxygen vacancies. In the catalytic membrane reactor, these oxygen vacancies are re-oxidized by gaseous CO_2 ($CO_{2,(g)}+V_O$ $CO_{(g)}+O^*_O$, Figure S6)[46,47] and penetrated oxygen from H_2O conversion on the core side. The high mobility of lattice oxygen over the CSO support and the chemical compatibility between the membrane and the CSO-Ni catalyst facilitate the rapid diffusion of oxygen species from the adsorption site to the three-phase boundary of the Ni sites, CSO support, and CH_4. This efficient diffusion is crucial for the oxidation of carbon produced from CH_4 conversion, ensuring that the catalytic process remains active and selective.

To optimize the overall process sustainability and energy utilization, while maximizing the H_2 production rate and facilitating carbon capture in the catalytic membrane reactor, the effluent gases (unconverted CH_4, H_2, CO, and CO_2) from the shell side were recirculated back into the reactor. This strategy ensures sustained participation of unreacted CH_4, H_2, CO, and CO_2 in the reforming process, thereby enhancing the overall conversion efficiency and elevating the CO_2 concentration. As shown in Figure S5B, continuous recirculation enables effective utilization of oxygen generated from water splitting on the core side, maintaining a high rate of methane conversion and minimizing the formation of undesired by-products. After 16 cycles of this recycling process, the methane concentration on the biogas reforming side was effectively reduced to zero. The final product CO_2 was ready for capture, while the CO concentration in the exhaust gas was measured to be 2.9% on the shell side. This low CO concentration does not affect the purity of the hydrogen produced via water splitting, ensuring the production of CO-free hydrogen. The hydrogen production rate, with an accumulative rate of 10.35 mL min^{-1} cm^{-2}, was achieved through the *in-situ* removal of the oxygen generated from water splitting on the core side. This rate corresponds to up to 94.5% (3.78 mol H_2/mol CH_4) of the theoretical hydrogen production value (4 mol H_2/mol CH_4), as shown in Figure 3D. 1 mL min^{-1} CO_2, 3 mL min^{-1} CH_4 and 16 mL min^{-1} N_2 were introduced into the shell side; 20 mL min^{-1} H_2O and 10 mL min^{-1} He were introduced into the core side. The notation "4 mol H_2/mol CH_4" indicates that when 1 mole of methane on the shell side is fully converted into CO_2 and H_2O, it requires 2 moles of oxygen. Concurrently, 4 moles of water (H_2O) on the core side undergo decomposition, yielding 4 moles of hydrogen gas. Compared with the reported literatures (Table S1), this hydrogen production rate is competitive with the highest values achieved in membrane reactors for water splitting. Notably, these previous studies were conducted with the exclusive presence of methane on the sweep side, whereas our simulated biogas contains both CO_2 and CH_4, which presents a more challenging environment. This comparison underscores the robustness and efficiency of our catalytic membrane reactor in handling real-world biogas compositions.

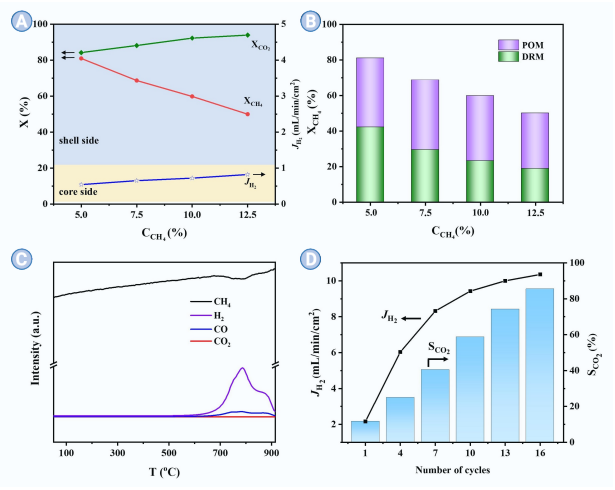

Figure 3. (A) Effects of CH_4 concentration in CSO-Ni@CSO-SSTF reactor. (B) The contribution of POM and DRM to methane conversion (X_{CH4}) in (A) calculated based on the CO_2 conversion. (C) CH_4-TPSR profiles of CSO-Ni catalyst. (D) The accumulative production rate of CO-free green hydrogen and accumulative selectivity of CO_2 in a CSO-Ni@CSO-SSAF reactor.

Catalytic stability. The stability of the CSO-Ni@CSO-SSTF catalytic membrane reactor was evaluated and compared with that of the Ni/Al_2O_3@CSO-SSTF, as depicted in Figure 4. Figures 4A & B reveal that the membrane reactor packed with the heterogeneous Ni/Al_2O_3 catalyst experienced a pronounced deactivation over a 100-hour operation period. Specifically, the CH_4 conversion rate plummeted from 27.1% to 11.8% (Figure 4B), while the H_2 production rate correspondingly decreased from 0.22 mL min^{-1} cm^{-2} to 0.02 mL min^{-1} cm^{-2} (Figure 4A). This significant decline in performance can be attributed to the inherent characteristics of the Ni/Al_2O_3 catalyst. The non-uniform distribution of active sites and the potential for coking or sintering of the Ni particles over extended periods can lead to a rapid loss of catalytic activity. Additionally, the physical separation between the catalyst and the membrane in this configuration may result in inefficient oxygen transport and utilization, further exacerbating the deactivation process. In stark contrast, the membrane reactor integrated with the homogeneous CSO-Ni catalyst demonstrated remarkable stability over the same 100-hour duration. It maintained a consistent CH_4 conversion rate of 62.8% and an H_2 production rate of 0.36 mL cm^{-2} min^{-1}. Notably, the initial hydrogen production rate in the CSO-Ni integrated membrane reactor was significantly higher than that in the Ni/Al_2O_3 packed reactor (0.36 mL cm^{-2} min^{-1} versus 0.22 mL min^{-1} cm^{-2}, Figure 4A). This superior performance can be ascribed to the unique synergistic interaction between the homogeneous CSO-Ni catalytic layer and the oxygen-permeable membrane, as illustrated in Figure 4C.

The homogeneous nature of the CSO-Ni catalyst ensures a uniform distribution of active sites, which enhances the overall catalytic efficiency. Moreover, the intimate integration of the CSO-Ni catalytic layer with the oxygen-permeable membrane facilitates the direct transport of reactive oxygen species to the active sites. This seamless interaction promotes a more efficient and rapid oxidation process, thereby sustaining high CH_4 conversion and H_2 production rates over extended periods. The enhanced oxygen transport kinetics in the CSO-Ni integrated reactor can be attributed to the elimination of the intermediate steps required in the Ni/Al_2O_3 reactor (Figure 4C). In the latter, oxygen ions transported to the membrane surface must first react to form molecular oxygen (O_2), which then diffuses through the gas phase to reach the active sites on the Ni/Al_2O_3 catalytic layer for participation in the POM reaction. This multi-step pathway not only limits the oxygen transport kinetics but also introduces additional potential points of failure or inefficiency in the overall reaction process. The CSO-Ni integrated reactor, by bypassing these intermediate steps, achieves a more direct and efficient utilization of oxygen, resulting in a higher initial hydrogen production rate and sustained performance over time.

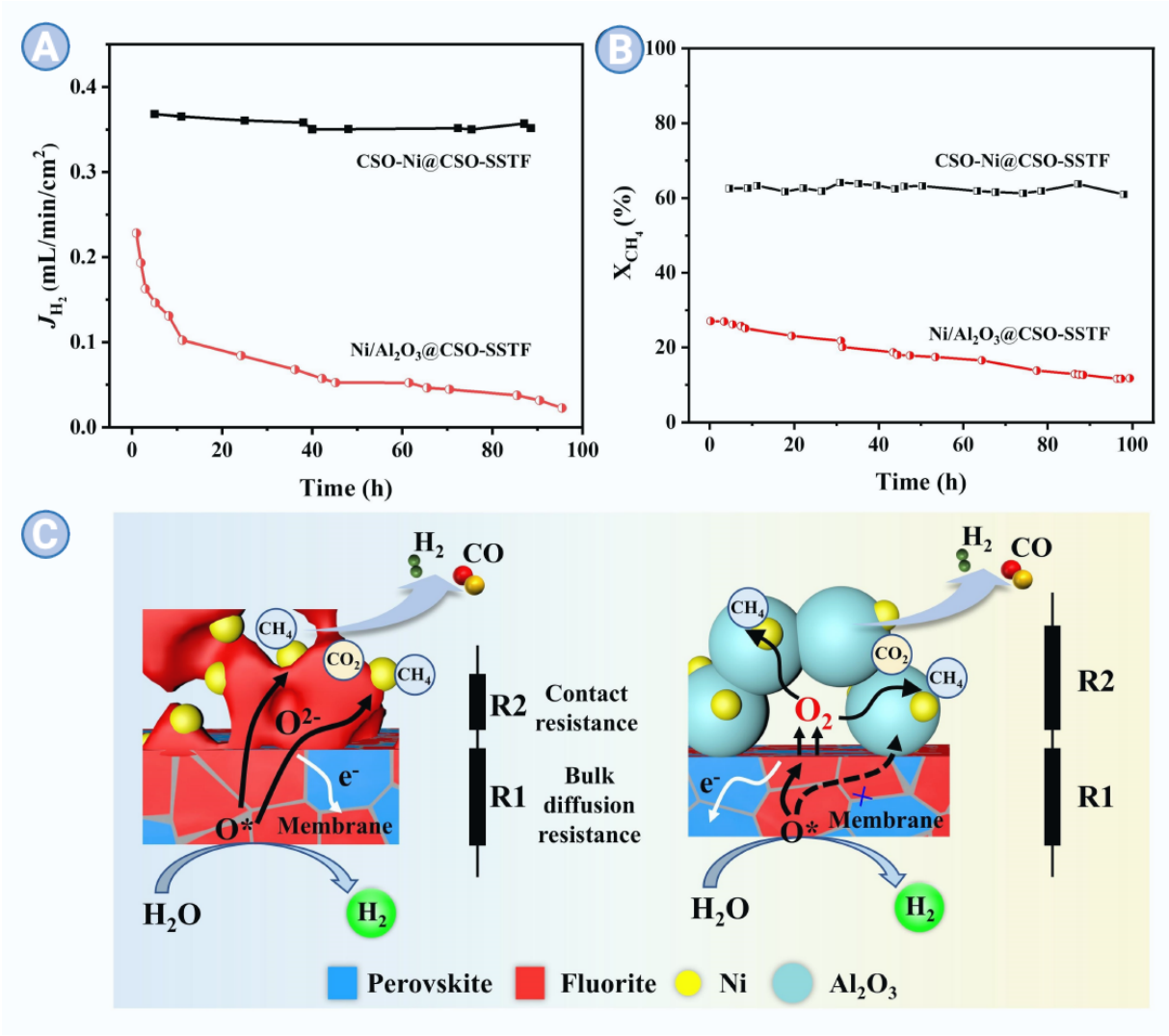

Figure 4. Long-term stability of the CSO-Ni@CSO-SSTF or the Ni/Al_2O_3@CSO-SSTF by coupling water splitting with biogas reforming at 930 °C. Shell side: 1.25 mL min^{-1} CO_2, 2.5 mL min^{-1} CH_4 and 16.25 mL min^{-1} N_2; Core side: 20 mL min^{-1} H_2O and 10 mL min^{-1} He. (A) Hydrogen production rate J_{H2}. (B) CH_4 conversion. (C) Schematic diagram of the biogas reforming on CSO-Ni or Ni/Al_2O_3 catalysts in the membrane reactor. R1: bulk diffusion resistance, R2: contact resistance.

To further elucidate the reasons behind the observed stability and performance of the different catalytic membrane reactors, a series of post-reaction characterizations were conducted on the catalytic layers and membranes after a 100-hour test period. Oxygen temperature programmed oxidation (O_2-TPO) measurements were performed to assess the extent of carbon deposition on the catalysts. The results revealed significant carbon deposition over the deactivated Ni/Al_2O_3 catalyst, as evidenced by the CO_2 desorption peak of 1.08 mmol $gcat^{-1}$ (Figure 5A).[48,49] This extensive coking is a common cause of catalyst deactivation in methane conversion processes, as it blocks the active sites and hinders the transport of reactants and products. In comparison, the CSO-Ni catalyst exhibited a much lower amount of coke deposition, with only 0.28 mmol $gcat^{-1}$ of CO_2 desorption observed. This indicates the improved oxygen transport in the homogeneous catalytic layer and the high stability of the *in-situ* exsolved Ni active sites, which are less prone to coking and sintering. The crystal structure of the spent CSO-SSTF membrane was analyzed by X-ray diffraction (XRD). As shown in Figure 5B, the surface of the spent membrane in contact with the Ni/Al_2O_3 catalyst exhibited significant changes in its crystal structure. The SSTF perovskite structure was found to be destroyed, and new phases such as TiO_2, $(Fe_{0.53}Al_{0.47})_2O_3$, and $Sr_3Al_2O_6$ appeared. These new phases are attributed to the reaction between the SSTF perovskite phase and the Ni/Al_2O_3 catalytic layer. This structural degradation was further confirmed by scanning electron microscopy (SEM) analysis, which revealed severe corrosion of the perovskite grains (Figure 5C). Such corrosion leads to a decrease in the oxygen permeation flux, thereby affecting the overall performance of the membrane reactor. Conversely, the spent membrane surface in contact with the CSO-Ni catalyst retained its original crystal structures, including the fluorite-type phase (JCPDS No. 75-0159) and perovskite phase (JCPDS No. 84-0443), with no detectable impurity peaks in the XRD pattern (Figure 5B). Additionally, no significant corrosion was observed even after 100 hours of operation at high temperatures, as confirmed by SEM analysis (Figure 5D). This indicates the excellent chemical stability and compatibility of the CSO-Ni catalyst with the SSTF membrane, which is crucial for maintaining the structural integrity and oxygen transport properties of the membrane. The average size of Ni nanoparticles in the CSO-Ni catalyst exhibited a slight increase to approximately 60 nm after undergoing a long-term stability test (Figure S7B). Although some aggregation of the metallic particles occurred, they remained well-dispersed on the fluorite surface and were still discernible in the XRD pattern (Figure S7D). This suggests that the Ni nanoparticles in the CSO-Ni catalyst are highly stable and resistant to sintering under the reaction conditions, which is essential for maintaining their catalytic activity over extended periods. Consequently, the CSO-SSTF catalytic membrane reactor, integrated with a homogeneous CSO-Ni catalytic layer, demonstrated enhanced oxygen transport and resistance to deactivation over time. This resulted in a simultaneous stable and active

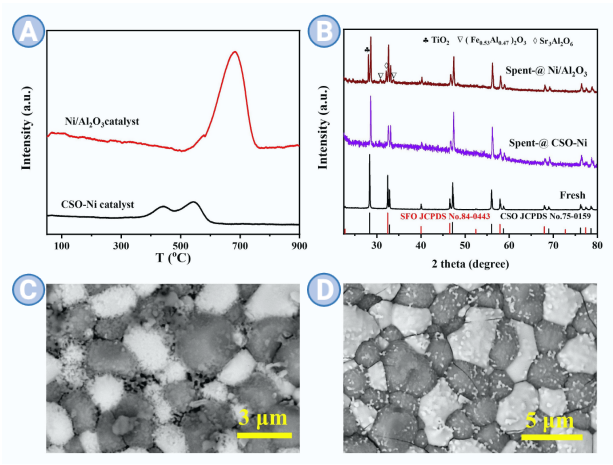

Figure 5. (A) The O_2-TPO profiles of the spent CSO-Ni and Ni/Al_2O_3 catalysts after long-term stability tests. (B) XRD patterns of the outer surface of fresh and spent membranes. SEM images of the surface of the spent membranes in contact with (C) Ni/Al_2O_3 and (D) CSO-Ni catalysts.

hydrogen production rate along with carbon capture. The improved performance can be attributed to the homogeneous distribution of active sites in the CSO-Ni catalyst, the efficient oxygen transport facilitated by the intimate integration of the catalyst and the membrane, and the excellent chemical stability and compatibility of the CSO-Ni catalyst with the SSTF membrane. These findings highlight the potential of the CSO-SSTF catalytic membrane reactor for sustainable and efficient hydrogen production from methane conversion processes.

CONCLUSIONS

In summary, this study presents a novel and highly efficient approach for the production of CO-free green hydrogen with negative CO_2 emissions through the utilization of a catalytic composite membrane reactor that integrates a dense ceria and perovskite membrane with a homogeneous porous $Ce_{0.8}Sm_{0.15}Ni_{0.05}O_{2-\delta}$ (CSO-Ni) catalytic layer. This innovative integration effectively addresses the critical challenges associated with catalyst and membrane compatibility, thereby significantly enhancing the efficiency and stability of the hydrogen production process. Through meticulous reactor optimization, the system achieves a low CO concentration of 4 ppm in the produced hydrogen while maintaining a high production rate of 10.35 mL min^{-1} cm^{-2} from water splitting, corresponding to 94.5% of the theoretical yield. This high efficiency can be attributed to the synergistic interaction between the dense ceria and perovskite membrane and the homogeneous CSO-Ni catalytic layer, which promotes efficient oxygen transport and water dissociation. Moreover, the concurrent capture of CO_2 with an 85.5% selectivity on the opposite side of the membrane underscores the system's capability for integrated carbon capture, contributing to negative CO_2 emissions. The enhanced stability of the reactor, demonstrated over a 100-hour continuous operation, is primarily attributed to the high coke resistance of the CSO-Ni catalyst, facilitated by the in situ exsolved Ni nanoparticles, and the excellent chemical compatibility between the catalyst and the membrane materials. This work represents a significant contribution to the field of chemical engineering, offering a practical and sustainable solution for hydrogen production that aligns with the global imperative for carbon neutrality. This work represents a significant milestone in the field of chemical engineering, offering a practical and sustainable solution for hydrogen production that aligns with the global imperative for carbon neutrality. The findings of this study pave the way for further research and development in sustainable hydrogen production technologies, with the potential to revolutionize the way we produce and utilize hydrogen as a clean energy carrier.

REFERENCES

1. Zhang S., Liu Y., Zhang M., et al. (2022). Sustainable Production of Hydrogen with High Purity from Methanol and Water at Low Temperatures. *Nat. Commun.* **13**:5527. DOI:10.1038/s41467-022-33186-z
2. Clark D., Malerød-Fjeld H., Budd M., et al. (2022). Single-Step Hydrogen Production from NH_3,CH_4, and Biogas in Stacked Proton Ceramic Reactors. *Science* **376**:390–393. DOI:10.1126/science.abj3951
3. Das S., Ashok J., Bian Z., et al. (2018). Silica-Ceria Sandwiched Ni Core-Shell Catalyst for Low Temperature Dry Reforming of Biogas: Coke Resistance and Mechanistic Insights. *Appl. Catal. B* **230**:220–236. DOI:10.1016/j.apcatb.2018.02.041
4. Liu L., Jiang P., Qian H., et al. (2022). CO_2-Negative Biomass Conversion: An Economic Route with Co-Production of Green Hydrogen and Highly Porous Carbon. *Appl. Energy* **311**:118685. DOI:10.1016/j.apenergy.2022.118685
5. Yan J. (2018). Negative-Emissions Hydrogen Energy. *Nat. Clim. Chang.* **8**:560–561. DOI:10.1038/s41558-018-0215-9
6. Liu Z., Shi S., Ji Y., et al. (2023). Opportunities of CO_2-Based Biorefineries for Production of Fuels and Chemicals. *Green Carbon* **1**:75–84. DOI:10.1016/j.greenca.2023.09.002
7. Alayoglu S., Nilekar A.U., Mavrikakis M., et al. (2008). Ru-Pt Core-Shell Nanoparticles for Preferential Oxidation of Carbon Monoxide in Hydrogen. *Nat. Mater.* **7**:333–338. DOI:10.1038/nmat2156
8. Chen L., Qi Z., Peng X., et al. (2021). Insights into the Mechanism of Methanol Steam Reforming Tandem Reaction over CeO_2 Supported Single-Site Catalysts. *J. Am. Chem. Soc.* **143**:12074–12081. DOI:10.1021/jacs.1c03895
9. Cheng H., Xia J., Wang M., et al. (2022). Surface Anion Promotes Pt Electrocatalysts with High CO Tolerance in Fuel-Cell Performance. *J. Am. Chem. Soc.* **144**:22018–22025. DOI:10.1021/jacs.2c09147
10. Voldsund M., Jordal K., Anantharaman R. (2016). Hydrogen Production with CO_2 Capture. *Int. J. Hydrogen Energy* **41**:4969–4992. DOI:10.1016/j.ijhydene.2016.01.009
11. Helf A., Cloete S., Keller F., et al. (2022). Carbon-Negative Hydrogen from Biomass Using Gas Switching Integrated Gasification: Techno-Economic Assessment. *Energy Convers. Manage.* **270**:114712. DOI:10.1016/j.enconman.2022.116248
12. Wang S., Yang H., Shi Z., et al. (2022). Renewable Hydrogen Production from the Organic Fraction of Municipal Solid Waste through a Novel Carbon-Negative Process Concept. *Energy* **252**:124056. DOI:10.1016/j.energy.2022.124056
13. Smith P., Davis S.J., Creutzig F., et al. (2015). Biophysical and Economic Limits to Negative CO_2 Emissions. *Nat. Clim. Chang.* **6**:42–50. DOI:10.1038/nclimate2870
14. Fuss S., Jones C.D., Kraxner F., et al. (2016). Research Priorities for Negative Emissions. *Environ. Res. Lett.* **11**:115007. DOI:10.1088/1748-9326/11/11/115007
15. Field C.B., Mach K.J. (2017). Rightsizing Carbon Dioxide Removal. *Science* **356**:706–707. DOI:10.1126/science.aam9726
16. Gao M., Fan J., Li X., et al. (2023). A Carbon-Negative Hydrogen Production Strategy: CO_2 Selective Capture with H_2 Production. *Angew. Chem. Int. Ed.* **62**:e202216527. DOI:10.1002/anie.202216527
17. Zhao Q., Su B., Wang H., et al. (2021). Mid/Low-Temperature Solar Hydrogen Generation Via Dry Reforming of Methane Enhanced in a Membrane Reactor. *Energy Convers. Manage.* **240**:114254. DOI:10.1016/j.enconman.2021.114254
18. Wang Y., Hu P., Yang J., et al. (2021). C-H Bond Activation in Light Alkanes: A Theoretical Perspective. *Chem. Soc. Rev.* **50**:4299–4358. DOI:10.1039/d0cs01262a
19. Kim S.M., Abdala P.M., Margossian T., et al. (2017). Cooperativity and Dynamics Increase the Performance of NiFe Dry Reforming Catalysts. *J. Am. Chem. Soc.* **139**:1937–1949. DOI:10.1021/jacs.6b11487
20. Wortman J., Igenegbai V.O., Almallahi R., et al. (2023). Optimizing Hierarchical Membrane/Catalyst Systems for Oxidative Coupling of Methane Using Additive Manufacturing. *Nat. Mater.* **22**:1523–1530. DOI:10.1038/s41563-023-01687-x
21. He G., Lan Q., Liu M., et al. (2023). Multilayered Ceramic Membrane with Ion Conducting Thin Layer Induced by Interface Reaction for Stable Hydrogen Production. *Angew. Chem. Int. Ed.* **62**:e202210485. DOI:10.1002/anie.202210485
22. Jia L., He G., Zhang Y., et al. (2021). Hydrogen Purification through Dual - Phase Oxygen Permeable Membrane with Excellent Stability. *Angew. Chem. Int. Ed.* **60**:5204–5208. DOI:10.1002/anie.202010184
23. Yang N.-T., Kathiraser Y., Kawi S. (2013). $La_{0.6}Sr_{0.4}Co_{0.8}Ni_{0.2}O_{3-\delta}$ Hollow Fiber Membrane Reactor: Integrated Oxygen Separation-CO_2 Reforming of Methane Reaction for Hydrogen Production. *Int. J. Hydrogen Energy* **38**: 4483-4491. DOI: 10.1016/j.ijhydene.2013.01.073.
24. Zhu N., Dong X., Liu Z., et al. (2012). Toward Highly-Effective and Sustainable Hydrogen Production: Bio-Ethanol Oxidative Steam Reforming Coupled with Water Splitting in a Thin Tubular Membrane Reactor. *Chem. Commun.* **48**:7137–7139. DOI:10.1039/c2cc30184a
25. Sivtsev V., Lapushkina E., Kovalev I., et al. (2023). Microtubular Solid Oxide Fuel Cells with a Two-Layer LSCF/BSCFM5 Cathode. *Green Carbon* **1**:154–159. DOI:10.1016/j.greenca.2023.11.002
26. Jiang H., Wang H., Werth S., et al. (2008). Simultaneous Production of Hydrogen and Synthesis Gas by Combining Water Splitting with Partial Oxidation of Methane in a Hollow-Fiber Membrane Reactor. *Angew. Chem. Int. Ed.* **47**:9341–9344. DOI:10.1002/anie.200803899
27. Evdou A., Zaspalis V., Nalbandian L. (2010). $La_{1-x}Sr_xFeO_{3-\delta}$ Perovskites as Redox Materials for Application in a Membrane Reactor for Simultaneous Production of Pure Hydrogen and Synthesis Gas. *Fuel* **89**:1265–1273. DOI:10.1016/j.fuel.2009.09.028
28. He G., Hu T., Zhou H., et al. (2017). Syngas Production by Biogas Reforming in a Redox-Stable and CO_2-Tolerant Oxygen Transporting Membrane Reactor. *Ind. Eng. Chem. Res.* **56**:10134–10141. DOI:10.1021/acs.iecr.7b01422
29. Liang W., Megarajan S.K., Liang F., et al. (2016). Coupling of N_2O Decomposition with CO_2 Reforming of CH_4 in Novel Cobalt-Free $BaFe_{0.9}Zr_{0.05}Al_{0.05}O_{3-\delta}$ Oxygen Transport

Membrane Reactor. *Chem. Eng. J.* **305**: 176-181. DOI: 10.1016/j.cej.2015.10.067.
30. Slade D.A., Duncan A.M., Nordheden K.J., et al. (2007). Mixed-Conducting Oxygen Permeable Ceramic Membranes for the Carbon Dioxide Reforming of Methane. *Green Chemistry* **9**:577–581. DOI:10.1039/b614232j
31. Wang H., Feldhoff A., Caro J., et al. (2009). Oxygen Selective Ceramic Hollow Fiber Membranes for Partial Oxidation of Methane. *AIChE J.* **55**:2657–2664. DOI:10.1002/aic.11856
32. Garcia-Fayos J., Lobera M.P., Balaguer M., et al. (2018). Catalyst Screening for Oxidative Coupling of Methane Integrated in Membrane Reactors. *Front. Mater.* **5**:31. DOI:10.3389/fmats.2018.00031
33. Cao Z., Jiang H., Luo H., et al. (2014). An Efficient Oxygen Activation Route for Improved Ammonia Oxidation through an Oxygen-Permeable Catalytic Membrane. *ChemCatChem* **6**:1190–1194. DOI:10.1002/cctc.201400048
34. Weng G., Ouyang K., Lin X., et al. (2022). Enhanced Hydrogen Permeability of Mixed Protonic-Electronic Conducting Membranes through an in - Situ Exsolution Strategy. *Adv. Funct. Mater.* **32**:2205255. DOI:10.1002/adfm.202205255
35. Xiao Y., Xie K. (2022). Active Exsolved Metal-Oxide Interfaces in Porous Single-Crystalline Ceria Monoliths for Efficient and Durable CH_4/CO_2 Reforming. *Angew. Chem. Int. Ed.* **61**:e202113079. DOI:10.1002/anie.202113079
36. Kim J.H., Kim J.K., Liu J., et al. (2021). Nanoparticle Ex-Solution for Supported Catalysts: Materials Design, Mechanism and Future Perspectives. *ACS Nano* **15**:81–110. DOI:10.1021/acsnano.0c07105
37. Tang Y., Wei Y., Wang Z., et al. (2019). Synergy of Single-Atom Ni1 and Ru1 Sites on CeO_2 for Dry Reforming of CH_4. *J. Am. Chem. Soc.* **141**:7283–7293. DOI:10.1021/jacs.8b10910
38. Huang J., Yan Y., Saqline S., et al. (2020). High Performance Ni Catalysts Prepared by Freeze Drying for Efficient Dry Reforming of Methane. *Appl. Catal. B* **275**:119109. DOI:10.1016/j.apcatb.2020.119109
39. Zhou R., Mohamedali M., Ren Y., et al. (2022). Facile Synthesis of Multi-Layered Nanostructured Ni/CeO_2 Catalyst Plus in-Situ Pre-Treatment for Efficient Dry Reforming of Methane. *Appl. Catal. B* **316**:121696. DOI:10.1016/j.apcatb.2022.121696
40. Ni Z., Djitcheu X., Gao X., et al. (2022). Effect of Preparation Methods of CeO_2 on the Properties and Performance of Ni/CeO_2 in CO_2 Reforming of CH_4. *Sci. Rep.* **12**:5344. DOI:10.1038/s41598-022-09291-w
41. Padi S.P., Shelly L., Komarala E.P., et al. (2020). Coke-Free Methane Dry Reforming over Nano-Sized $NiO-CeO_2$ Solid Solution after Exsolution. *Catal. Commun.* **138**:105951. DOI:10.1016/j.catcom.2020.105951
42. Liu Z., Zhang F., Rui N., et al. (2019). Highly Active Ceria-Supported Ru Catalyst for the Dry Reforming of Methane: In Situ Identification of Ru^{0+}–Ce^{3+} Interactions for Enhanced Conversion. *ACS Catalysis* **9**:3349–3359. DOI:10.1021/acscatal.8b05162
43. Hussien A.G.S., Damaskinos C.M., Dabbawala A.A., et al. (2022). Elucidating the Role of La^{3+}/Sm^{3+} in the Carbon Paths of Dry Reforming of Methane over Ni/Ce-La(Sm)-Cu-O Using Transient Kinetics and Isotopic Techniques. *Appl. Catal. B* **304**:121015. DOI:10.1016/j.apcatb.2021.121015
44. Khajonvittayakul C., Tongnan V., Kangsadan T., et al. (2019). Thermodynamic and Mechanism Study of Syngas Production Via Integration of Nitrous Oxide Decomposition and Methane Partial Oxidation in the Presence of 10%NiO-$La_{0.3}Sr_{0.7}Co_{0.7}Fe_{0.3}O_{3-\delta}$. *React. Kinet. Mech. Catal.* **127**: 839-855. DOI: 10.1007/s11144-019-01600-1.
45. Salcedo A., Iglesias I., Mariño F., et al. (2018). Promoted Methane Activation on Doped Ceria Via Occupation of Pr(4f) States. *Appl. Surf. Sci.* **458**:397–404. DOI:10.1016/j.apsusc.2018.07.090
46. Bhavani A.G., Kim W.Y., Lee J.S. (2013). Barium Substituted Lanthanum Manganite Perovskite for CO_2 Reforming of Methane. *ACS Catal.* **3**:1537–1544. DOI:10.1021/cs400245m
47. Wang Y., Zhang R., Yan B. (2022). $Ni/Ce_{0.9}Eu_{0.1}O_{1.95}$ with Enhanced Coke Resistance for Dry Reforming of Methane. *J. Catal.* **407**: 77-89. DOI: 10.1016/j.jcat.2022.01.020
48. Teh L.P., Setiabudi H.D., Timmiati S.N., et al. (2021). Recent Progress in Ceria-Based Catalysts for the Dry Reforming of Methane: A Review. *Chem. Eng. Sci.* **242**:116606. DOI:10.1016/j.ces.2021.116606
49. Xie T., Zhao X., Zhang J., et al. (2015). Ni Nanoparticles Immobilized Ce-Modified Mesoporous Silica Via a Novel Sublimation-Deposition Strategy for Catalytic Reforming of Methane with Carbon Dioxide. *Int. J. Hydrogen Energy* **40**:9685–9695. DOI:10.1016/j.ijhydene.2015.06.008

FUNDING AND ACKNOWLEDGMENTS

This work was financially supported by National Key R&D Program of China (2022YFB3805503), National Natural Science Foundation of China (22175193, 22261132517, 22108286), Youth Innovation Promotion Association CAS (Grant No. 2022210), and QIBEBT (S202306). The funders had no role in study design, data collection and analysis, decision to publish, or preparation of the manuscript.

AUTHOR CONTRIBUTIONS

Mengke Liu: Investigation, Data curation, Writing – original draft. Tianmiao Hu: Validation, Methodology. Yan Zhang: Supervision, Conceptualization, Funding acquisition, Methodology, Writing – review & editing. Zhengwen Cao: Supervision, Conceptualization, Funding acquisition, Writing – review & editing. Lujian Jia: Validation, Data curation. Wenyuan Liang: Validation, Methodology. Alexander Nemudry: Writing – review & editing. Heqing Jiang: Supervision, Conceptualization, Funding acquisition, Methodology, Writing – review & editing, Project administration, Resources.

DECLARATION OF INTERESTS

The authors declare no competing interests.

DATA AND MATERIALS AVAILABILITY

All data are available from the lead contact upon reasonable request.

SUPPLEMENTAL INFORMATION

It can be found online at https://doi.org/10.59717/j.xinn-energy.2025.100119